**Supporting Information**

# Underlying mechanism of CO$_2$ adsorption onto conjugated azacyclo-copolymers: N-doped adsorbents capture CO$_2$ chiefly through acid-base interaction?

Shi-Chao Qi, Ju-Kang Wu, Jie Lu, Guo-Xing Yu, Rong-Rong Zhu, Yu Liu, Xiao-Qin Liu and Lin-Bing Sun*

State Key Laboratory of Materials-Oriented Chemical Engineering, Jiangsu National Synergetic Innovation Center for Advanced Materials (SICAM), College of Chemical Engineering, Nanjing Tech University, Nanjing 211816, China

*Corresponding author. E-mail: lbsun@njtech.edu.cn

**Supplementary Tables**

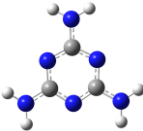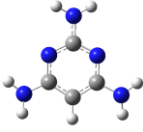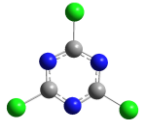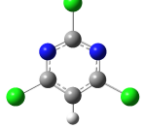**Table S1.** Zero-point energies of first-principle optimized geometries of four monomers and HCl.
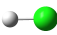
| Material | Geometry | Zero-point energy (Hartree) |
|---|---|---|
| 3AM |  | -446.073235 |
| 2AM |  | -430.016216 |
| 3CL |  | -1658.476871 |
| 2CL |  | -1642.441762 |
| HCl |  | -460.645646 |

**Table S2.** Formation potential of first-principle optimized geometry of dimer composed by 3AM and 3CL.
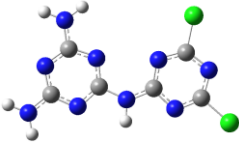
| Dimer | Geometry | Zero-point energy (Hartree) | Formation potential (kcal/mol) |
|---|---|---|---|
| 3AM-3CL |  | -1643.926612 | -13.9 |

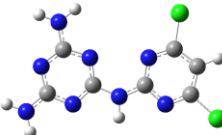**Table S3.** Formation potentials of first-principle optimized geometries of dimers composed by 3AM and 2CL.

| Dimer | Geometry | Zero-point energy (Hartree) | Formation potential (kcal/mol) |
|---|---|---|---|
| 3AM-2CL-1 |  | -1627.887557 | -11.4 |
| 3AM-2CL-2 |  | -1627.881985 | -7.9 |
| 3AM-2CL-3 |  | -1627.893908 | -15.4 |

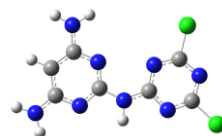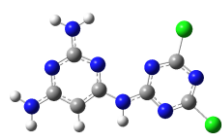**Table S4.** Formation potentials of first-principle optimized geometries of dimers composed by 2AM and 3CL.

| Dimer | Geometry | Zero-point energy (Hartree) | Formation potential (kcal/mol) |
|---|---|---|---|
| 2AM-3CL-1 |  | -1627.872282 | -15.6 |
| 2AM-3CL-2 |  | -1627.870239 | -14.3 |
| 2AM-3CL-3 |  | -1627.881204 | -21.2 |

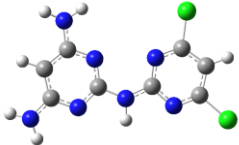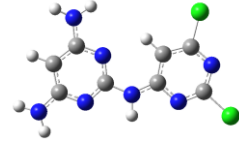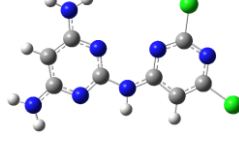**Table S5.** Formation potentials of first-principle optimized geometries of dimers composed by 2AM and 2CL.
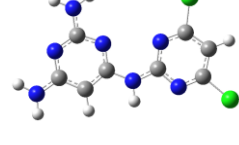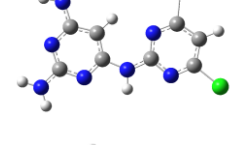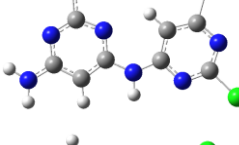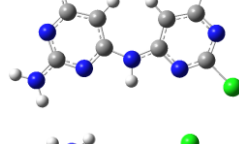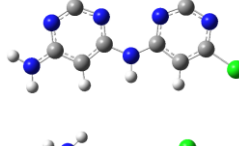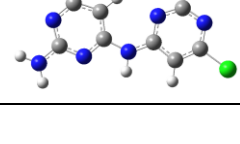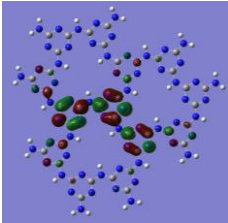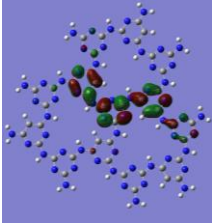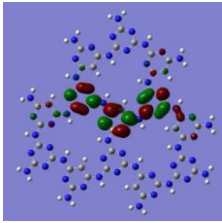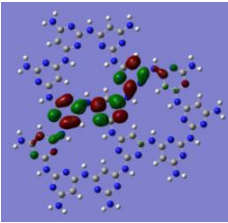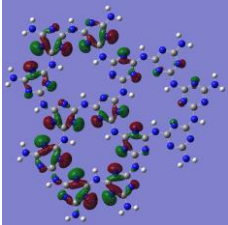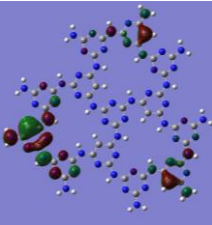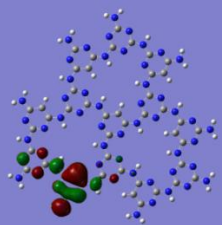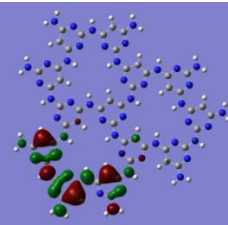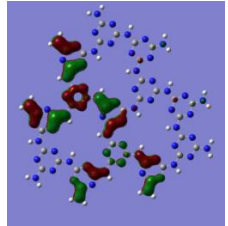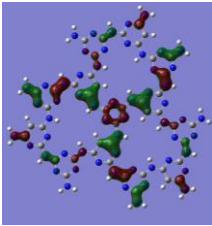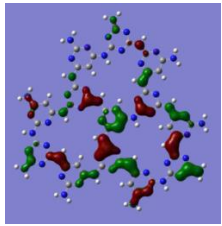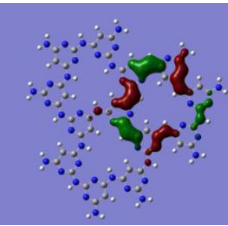
| Dimer | Geometry | Zero-point energy (Hartree) | Formation potential (kcal/mol) |
|---|---|---|---|
| 2AM-2CL-1 |  | -1611.832803 | -12.8 |
| 2AM-2CL-2 |  | -1611.839248 | -16.9 |
| 2AM-2CL-3 |  | -1611.827444 | -9.5 |
| 2AM-2CL-4 |  | -1611.830772 | -11.6 |
| 2AM-2CL-5 |  | -1611.841832 | -18.5 |
| 2AM-2CL-6 |  | -1611.837980 | -16.1 |
| 2AM-2CL-7 |  | -1611.833275 | -13.1 |
| 2AM-2CL-8 |  | -1611.824042 | -7.3 |
| 2AM-2CL-9 |  | -1611.837260 | -15.6 |

**Table S6.** Textural characteristics and elemental contents of the samples.

| Copolymer | $S_{BET}$ (m²/g) | $V_{pore}$ (cm³/g) | Theoretical N content (%, wt) | Elemental analysis (%, wt) | | | |
|---|---|---|---|---|---|---|---|
| | | | | C | H | N | O and ash |
| 3AM3CL | 894 | 0.864 | 62.7 | 34.2 | 2.2 | 59.4 | 4.2 |
| 3AM2CL | 196 | 0.601 | 56.0 | 37.8 | 2.8 | 53.2 | 6.2 |
| 2AM3CL | 105 | 0.535 | 56.0 | 39.5 | 3.3 | 52.3 | 4.9 |
| 2AM2CL | 47 | 0.347 | 49.2 | 43.9 | 3.7 | 46.8 | 5.6 |

**Table S7.** The energies of LUMO (π*)[a], HOMO[b], and highest occupied conjugated-π orbital of copolymers.

| Orbital | 3AM3CL | 3AM2CL | 2AM3CL | 2AM2CL |
|---|---|---|---|---|
| LUMO (π*) | | | | |
| $E_{LUMO}$/eV | -1.66 | -1.68 | -1.87 | -1.59 |
| HOMO | | | | |
| $E_{HOMO}$/eV | -5.00 | -4.74 | -4.69 | -4.30 |
| Conjugated π | | | | |
| $E_\pi$/eV | -8.56 | -8.84 | -9.08 | -9.46 |
| $\Delta E$ (π*-π)/eV | 6.89 | 7.15 | 7.21 | 7.87 |

[a] LUMO, lowest unoccupied molecular orbital; [b] HOMO, highest occupied molecular orbital.

**Table S8.** Parameters for the derivation of functional relationship between $C_{ads}$ and $D_{neg}$ at 0 °C and 25 °C.

| Adsorbent | $\varepsilon$ [a] | $S_{BET}$ (m²/g) | $\sigma$ ($10^{-19}$ m²) [b] | $D_{neg}$ (mmol/g) [c] | $C_{ads,0}$ (mmol/g) | $C_{ads,25}$ (mmol/g) |
|---|---|---|---|---|---|---|
| **3AM3CL** | 3 | 894 | 6.573 | 6.775 | 3.10 | 2.01 |
| **3AM2CL** | 2 | 196 | 6.678 | 0.975 | 1.21 | 0.60 |
| **2AM3CL** | 2 | 105 | 6.810 | 0.512 | 1.10 | 0.56 |
| **2AM2CL** | 1 | 47 | 6.891 | 0.113 | 0.99 | 0.52 |

[a] $\varepsilon$, the masking factor for each copolymer indicating the average number of unshielded negative ESP sites in a triangular intramolecular cave ($\varepsilon$ = 3, 2, 2, and 1 for 3AM3CL, 3AM2CL, 2AM3CL, and 2AM2CL, respectively); [b] $\sigma$, the first-principle calculated average area of one hexagonal structure in corresponding copolymer (m²); [c] $D_{neg}$, the effective density of the negative potential sites on the interface.


**Table S9.** Negative ESP extremum of representative N-based $CO_2$ adsorption sites calculated with first-principle.

| N-based $CO_2$ adsorption site | Negative ESP extremum (eV) |
|---|---|
| $NH_3$ | −0.070 |
| $NH_2NH_2$ | −0.058 |
| $H_2NCH_2CH_2NH_2$ | −0.064 |
| $Et_2NH$ | −0.051 |
| $Et_3N$ | −0.042 |
| Aniline | −0.033 |
| Indole | −0.035 |
| Pyridine | −0.059 |
| Quinoline | −0.056 |


**Table S10.** Textural properties of the SU-MAC adsorbents of Ref. 45 and the estimated effective N content.

| Materials | $S_{BET}$ | N content | $CO_2$ capacity at 298K | $S_{BET}$ ratio | Effective N content ratio [a] | $CO_2$ capacity ratio |
|---|---|---|---|---|---|---|
| | m² g⁻¹ | %, wt | mmol g⁻¹ | | | |
| SU-MAC-500 | 941 | 5.8 | 4.50 | 0.397 | 0.720 | 1.447 |
| SU-MAC-600 | 1500 | 4.0 | 4.18 | 0.633 | 0.791 | 1.344 |
| SU-MAC-800 | 2369 | 3.2 | 3.11 | 1.000 | 1.000 | 1.000 |

a, Effective N content ratio is estimated through N content multiplying by $S_{BET}$ ratio.
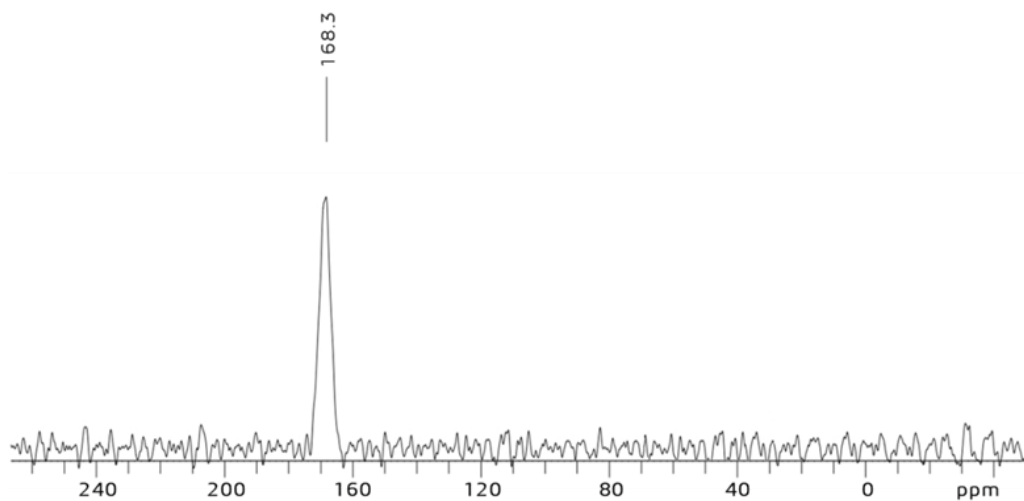
# Supplementary Figures



**Fig. S1.** Solid state $^{13}$C-NMR spectrum of 3AM3CL. $\delta$ = 168.3 ppm, C atoms of triazine rings bonding –NH–.
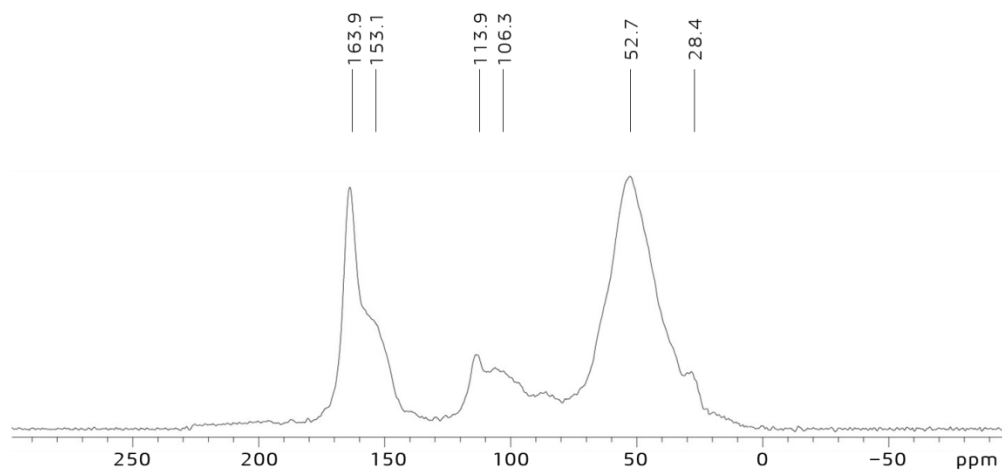


**Fig. S2.** Solid state $^{13}$C-NMR spectrum of 3AM2CL. $\delta$ = 163.9 and 153.1 ppm, C atoms bonding –NH–; $\delta$ = 113.9, 106.3, 52.7, and 28.4 ppm, 5'-C atoms of pyrimidine rings.

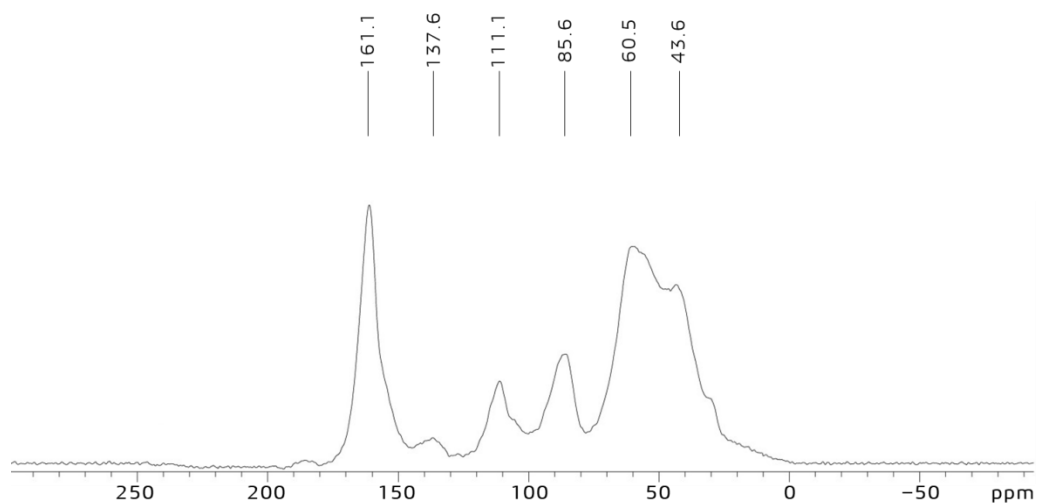**Fig. S3.** Solid state $^{13}$C-NMR spectrum of 2AM3CL. $\delta$ = 161.1 and 137.6 ppm, C atoms bonding –NH–; $\delta$ = 111.1, 85.6, 60.5, and 43.6 ppm, *5'*-C atoms of pyrimidine rings.



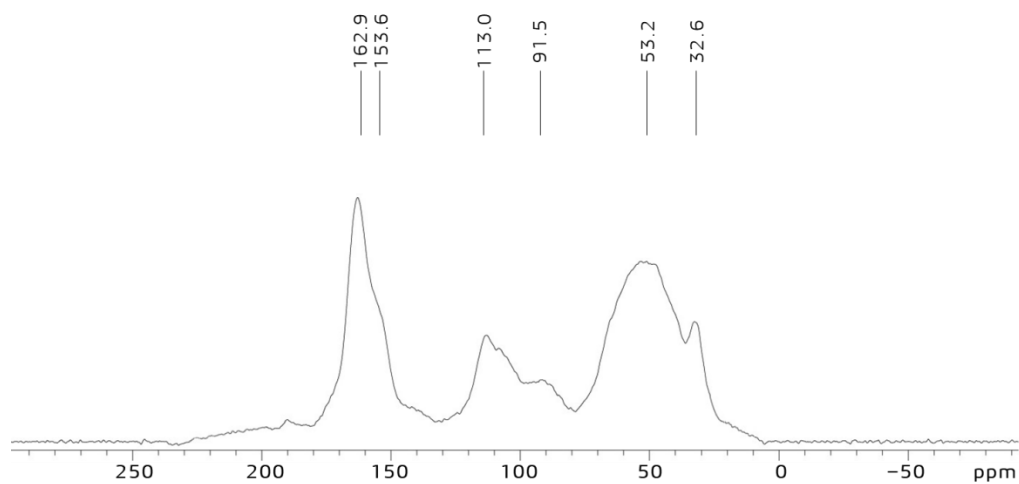**Fig. S4.** Solid state $^{13}$C-NMR spectrum of 2AM2CL. $\delta$ = 162.9 and 153.6 ppm, C atoms bonding –NH–; $\delta$ = 113.0, 91.5, 53.2, and 32.6 ppm, *5'*-C atoms of pyrimidine rings.
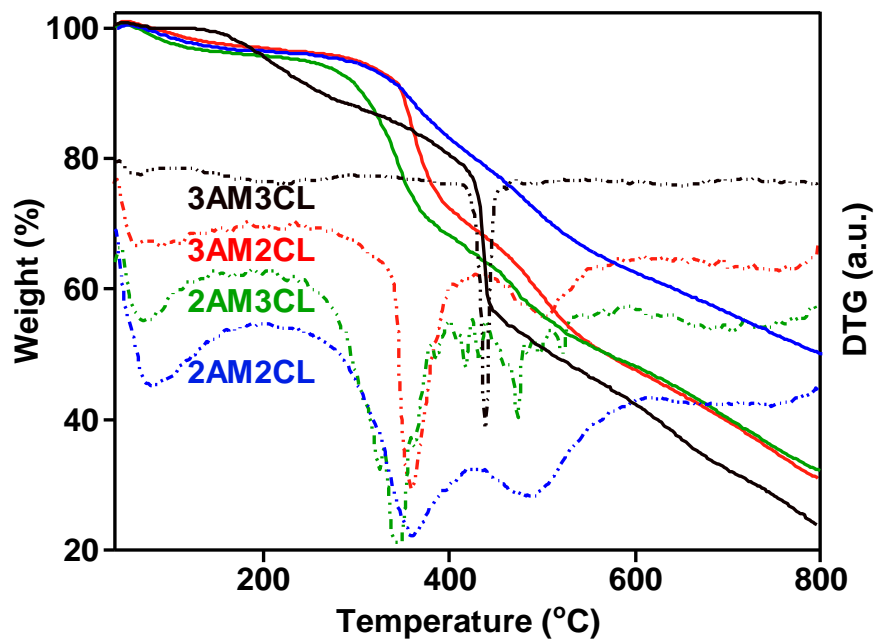
**Fig. S5.** TG and DTG profiles of four copolymers.
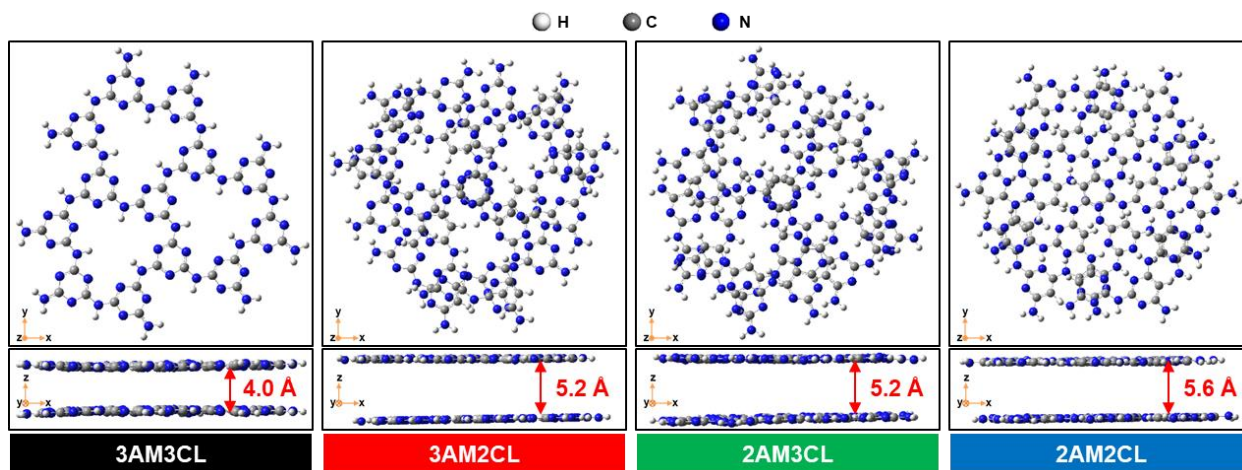


**Fig. S6.** The representative configuration of interaction between two interlayers of a copolymer.
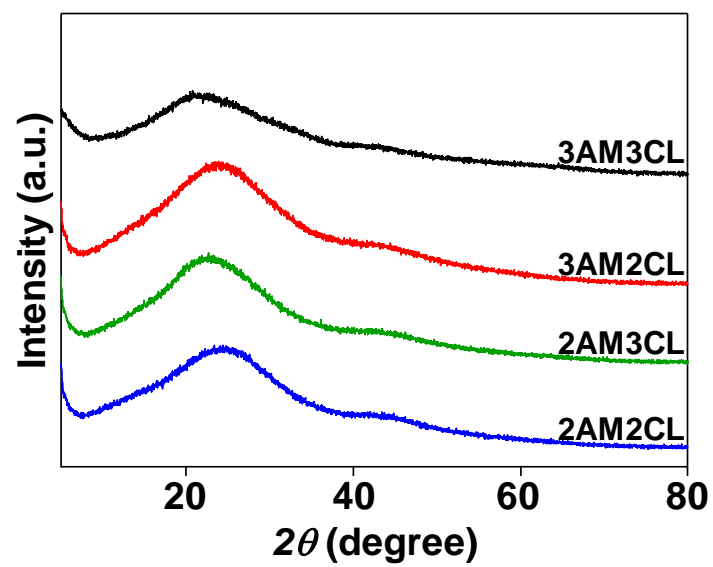
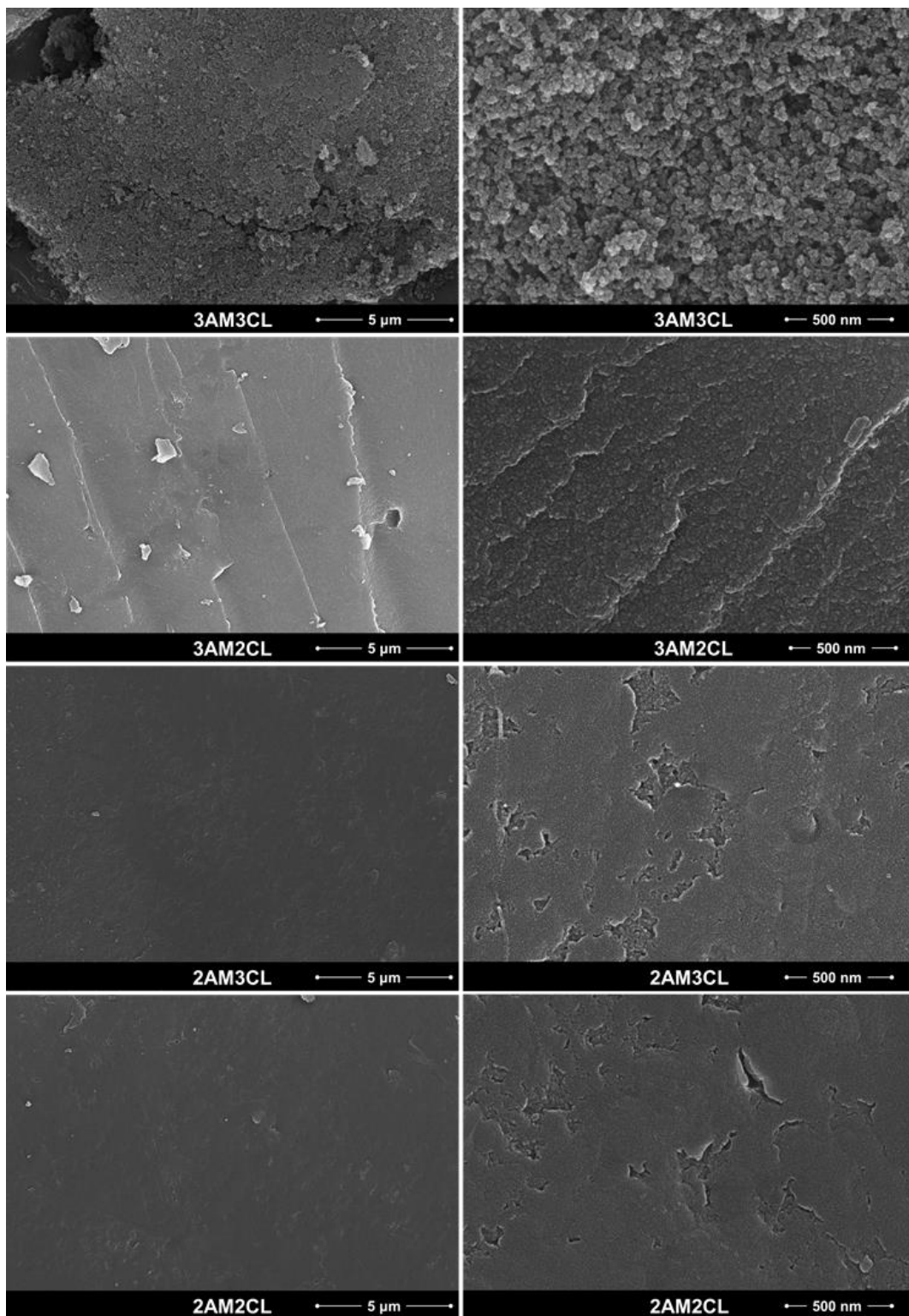**Fig. S7.** XRD patterns of four copolymers.

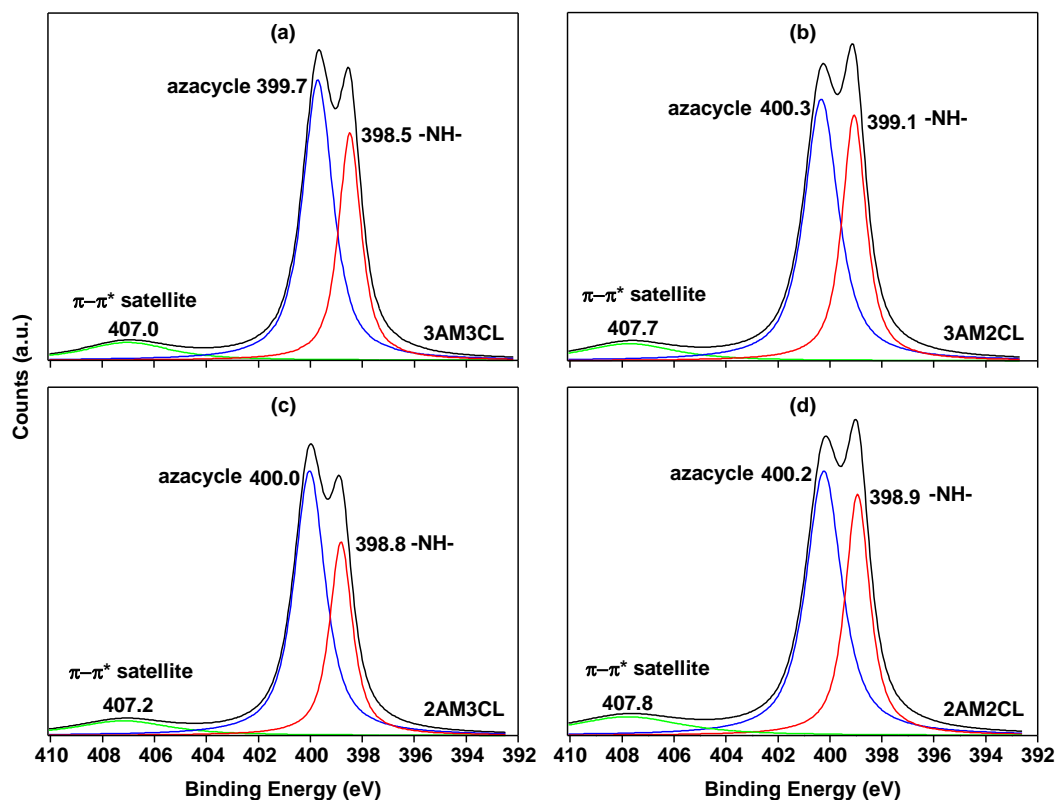**Fig. S8.** SEM images of four copolymers.

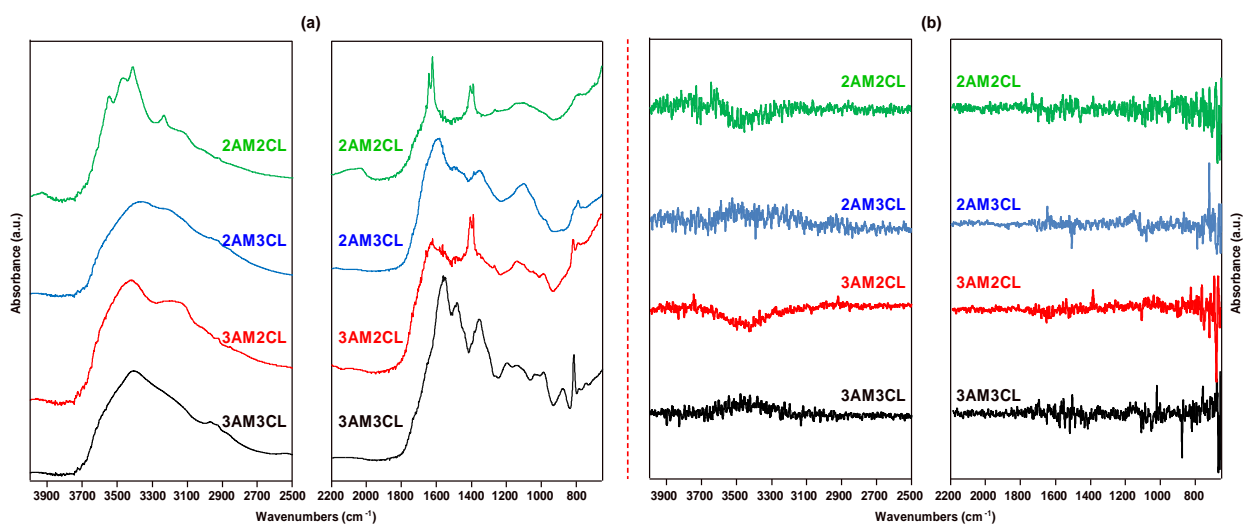**Fig. S9.** XPS spectra for N1s of four copolymers.



**Fig. S10.** In-situ DRFTIR spectra of the copolymers (a) and those of net changes after $CO_2$ adsorption (b). With taken those of the copolymers as background spectra, the in-situ DRFTIR spectra of net changes for the copolymers were recorded after vacuum treatment at 85 °C for 2 h, and the subsequent sufficient gas replacement by $CO_2$ at 2 bar and 25 °C.
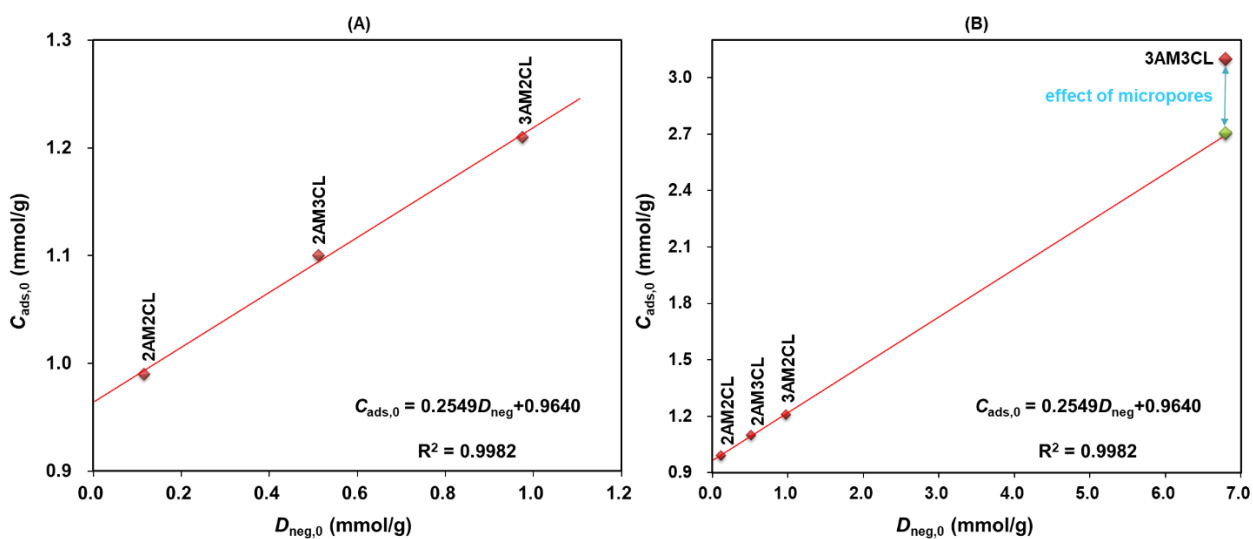
**Fig. S11.** (A) Fitted functional relationship between $C_{ads,0}$ at 0 °C and $D_{neg}$ based on 3AM2CL, 2AM3CL, and 2AM2CL; and (B) the risen $C_{ads,0}$ caused by micropores of 3AM3CL.
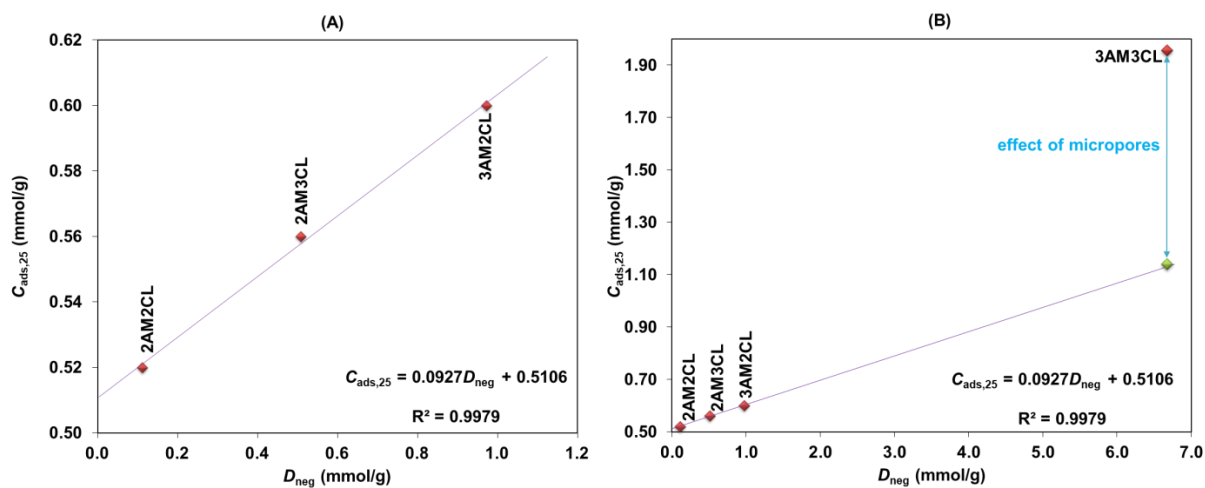


**Fig. S12.** (A) Fitted functional relationship between $C_{ads,25}$ at 25 °C and $D_{neg}$ based on 3AM2CL, 2AM3CL, and 2AM2CL; and (B) the risen $C_{ads,25}$ caused by micropores of 3AM3CL.
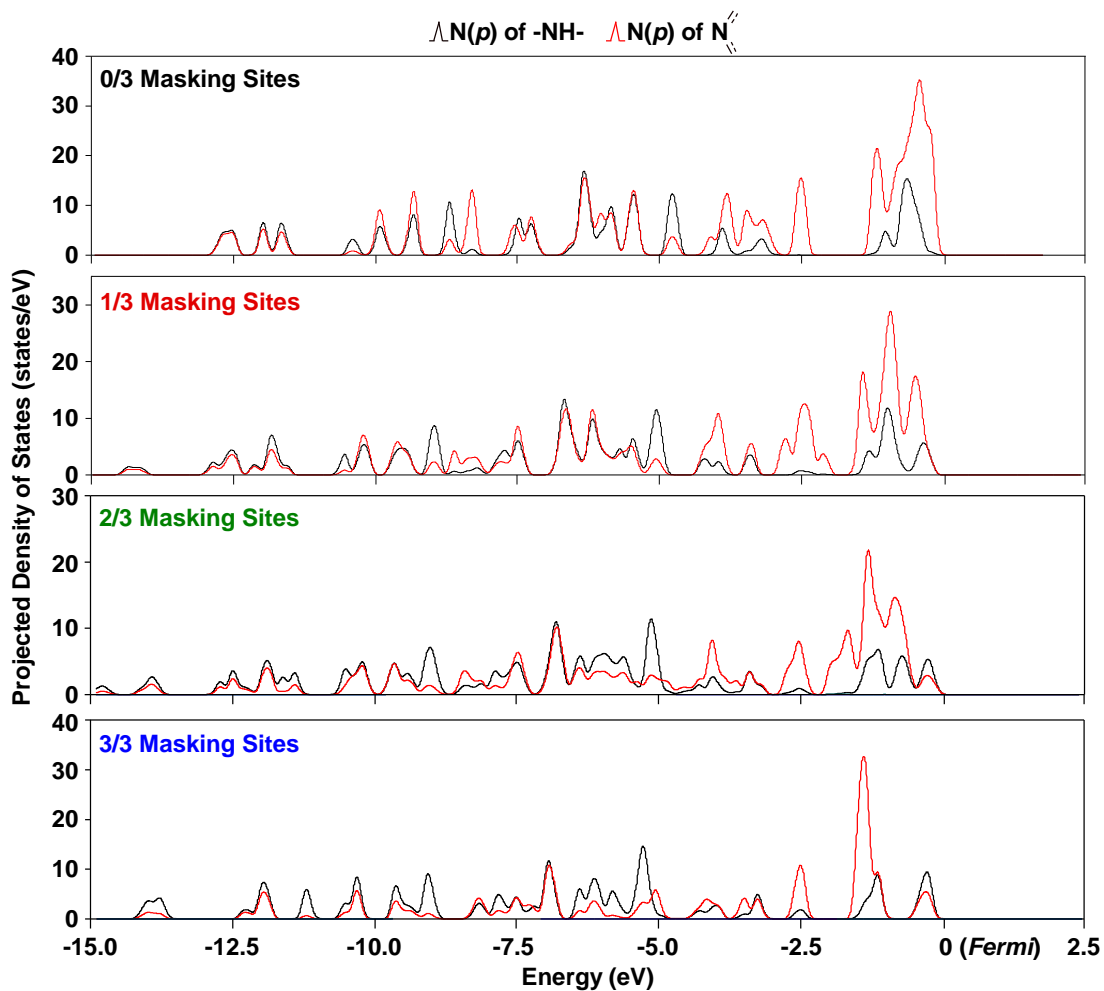
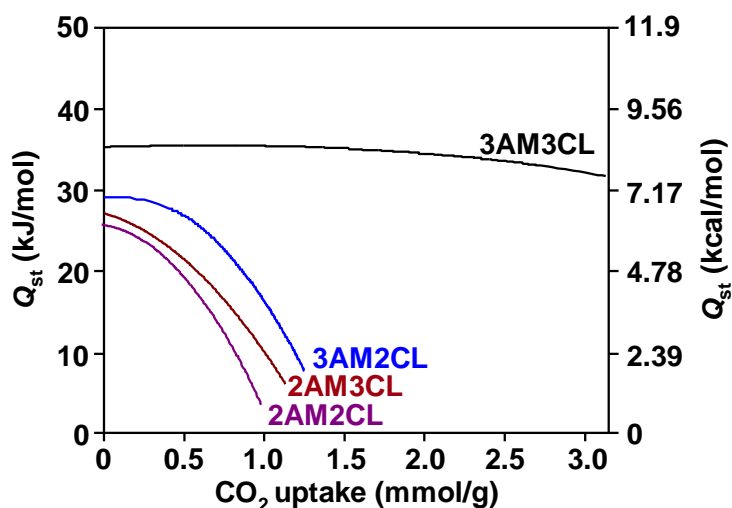**Fig. S13.** Projected density of states of 0/3, 1/3, 2/3, and 3/3 Masking Sites.



**Fig. S14.** Isosteric heats ($Q_{st}$) of $CO_2$ adsorption over the four copolymers. $Q_{st}$ were calculated from the data of $CO_2$ uptake at the temperatures of 0 °C and 25 °C, fitted with a virial-type expression.
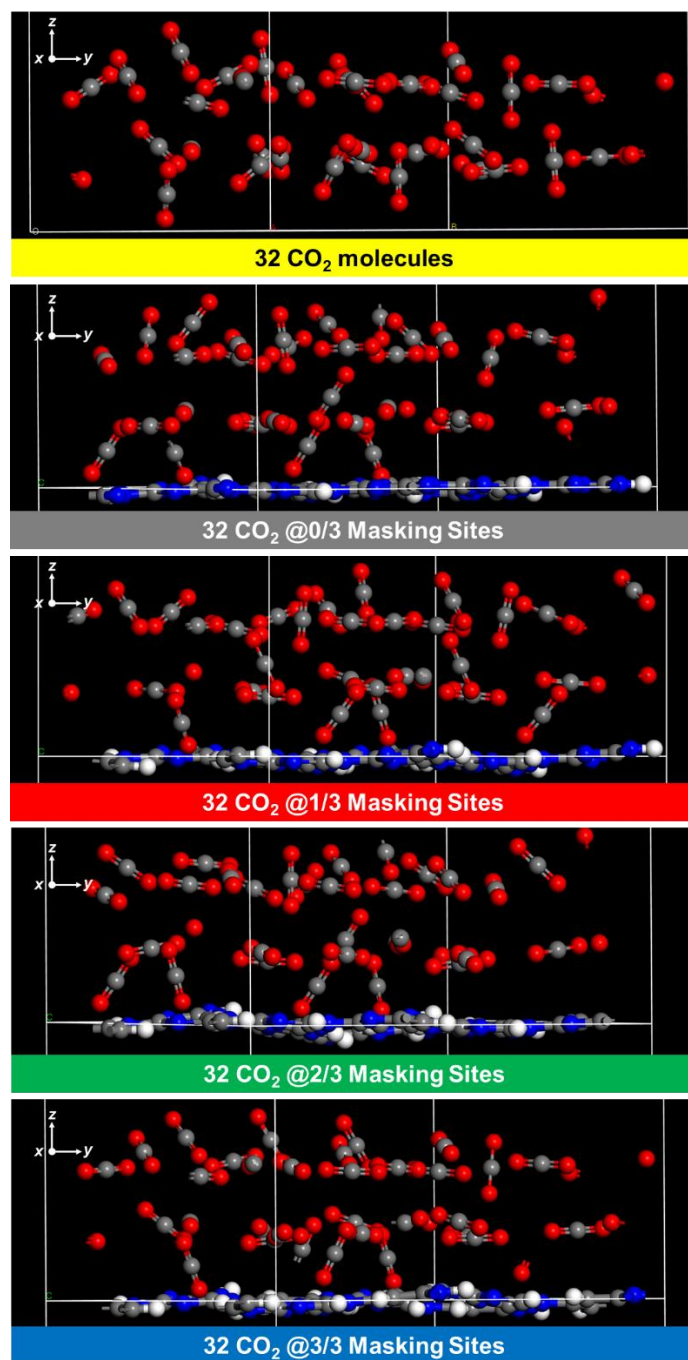
**Fig. S15.** The condensed states of 32 $CO_2$ molecules onto different Masking Sites.
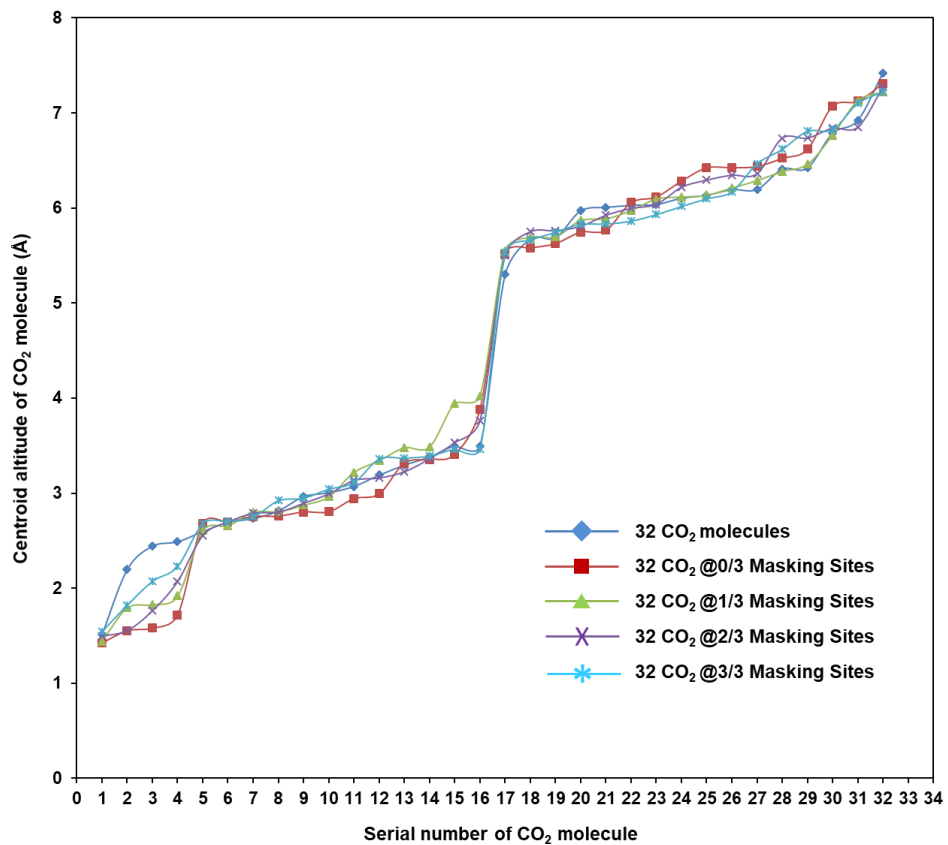
**Fig. S16.** The centroid altitude distribution of 32 $CO_2$ molecules onto different Masking Sites.
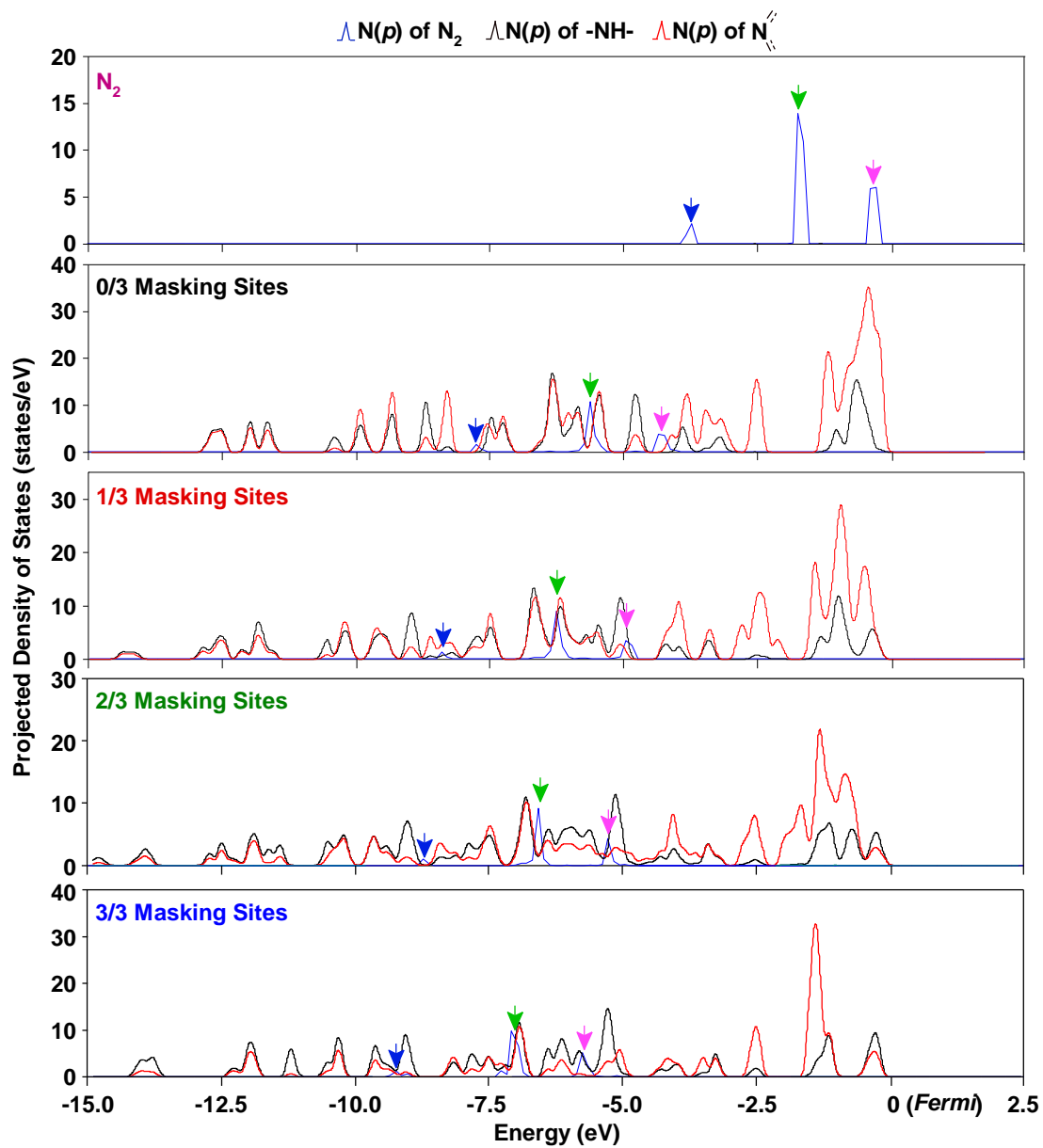
**Fig. S17.** Projected density of states of $N_2$ molecule adsorbed on the 0/3, 1/3, 2/3, and 3/3 Masking Sites.